The following publication Z. Fang, Y. Chen, H. Wu, Z. Li and C. Lu, "Short-Chirped-Pulse OFDR Assisted by Negative Quality Factor Analysis of Correlation for Adaptive Distributed Acoustic Sensing," in Journal of Lightwave Technology, vol. 43, no. 8, pp. 3777-3785, 15 April, 2025 is available at https://doi.org/10.1109/JLT.2025.3526787.

Short-Chirped-Pulse OFDR Assisted by Negative Quality Factor Analysis of Correlation for Adaptive Distributed Acoustic Sensing

Zheng Fang, Yingyu Chen, Huan Wu, Zhaohui Li, and Chao Lu

***Abstract*—We propose a distributed acoustic sensing technique that utilizes correlation analysis derived from short-chirped-pulse optical frequency-domain reflectometry (OFDR). The performance of the technique is enhanced by negative quality factor (NQF) analysis, which evaluates the reliability of Rayleigh backscattering spectra (RBS) shift readings under vibration. By selectively filtering out valid RBS shift data, we can overcome the intensity response range limitations typically imposed by the sweeping range. Using this approach, we have successfully demonstrated the detection of maximum vibration frequencies up to 1 kHz over a 32 km fiber under test, achieving a signal-to-noise ratio (SNR) of up to 30 dB and a spatial resolution of 14 m. Furthermore, the system's ability to sense vibrations, particularly those of unexpectedly large magnitudes, has been confirmed.**

***Index Terms*—Distributed acoustic sensing, optical frequency domain reflectometry, negative quality factor.**

I. Introduction

DISTRIBUTED optical fiber sensors (DOFS) have become a preferred choice for large-scale structural health monitoring in recent years [1-3]. Among these, distributed acoustic sensors (DAS) have generated significant research interest due to their broad applicability and practical effectiveness [4,5]. This interest is driven by the ability of DAS to characterize the physical condition of a structure or detect environmental perturbations through intrinsic or external acoustic signals. Unlike distributed vibration sensors (DVS), DAS can detect not only vibration events but also analyze the vibration data, extracting details such as frequency and intensity. With their distributed measurement capabilities, exceptional acoustic signal sensitivity, and long measurement range, DAS systems have been deployed in applications such as safety monitoring of railway [6,7], border surveillance [8], and pipeline leakage detection [9,10].

Currently, the most widely used DAS configuration is phase-sensitive optical time-domain reflectometry (Φ-OTDR) [11-14], which operates on the principle of optical time-domain reflectometry (OTDR). Enhancements in amplification technology and phase noise compensation [15,16] have enabled Φ-OTDR to perform distributed acoustic sensing over distances of hundreds of kilometers. However, OTDR-based systems inherently face a trade-off between maximum sensing range and spatial resolution. Specifically, achieving high spatial resolution necessitates the use of narrow probe pulses, which reduces optical power and, consequently, the sensing range—and vice versa. To address this challenge, researchers have turned to DOFS based on optical frequency-domain reflectometry (OFDR). OFDR-based systems also utilize Rayleigh backscattering for acoustic signal detection, but unlike OTDR, they analyze frequency-domain information through the use of linear-frequency modulated incident light. OFDR has proven its superior performance in stationary measurements of deformation, strain, and temperature [17]. However, its application in dynamic measurements remains underexplored because conventional OFDR systems use tunable laser sources (TLS) with large sweeping ranges (tens of nanometers) and long sweeping periods (hundreds of microseconds), which limits their ability to capture rapidly changing signals over time.

Several techniques have been proposed to facilitate dynamic measurements in OFDR-based systems. For instance, a time-resolved OFDR approach has been examined for dynamic measurement, achieving a frequency range of 0-32 Hz with a spatial resolution of 10 cm over a 17 m fiber span [18]. However, the measurement range is constrained by the short coherence length of the TLS, and the frequency response is limited by the slow tuning process. In another correlation-based OFDR system [19], the location and vibration frequency are determined through cross-correlation in the frequency domain. Although the measurement range is extended to 12 km, this scheme only considers the amplitude term, leading to incomplete vibration information recovery. In contrast, a time-gated digital OFDR (TGD-OFDR) [20] uses the phase term of the Rayleigh backscattering signal to directly restore the vibration signal, significantly extending the measurement range

This work was supported by Guangdong S&T Programme (2024B0101030001), The Research Grants Council (RGC) of Hong Kong General Research Fund (GRF: PolyU 15227321), and The Hong Kong Ph.D. Fellowship. (Corresponding author: Zheng Fang)

Zheng Fang, Huan Wu and Chao Lu are with the Department of Electrical and Electronic Engineering, The Hong Kong Polytechnic University, Hong Kong (e-mail: zheng-eie.fang@connect.polyu.hk; hkpolyu.wu@polyu.edu.hk; chao.lu@polyu.edu.hk)

Yingyu Chen and Zhaohui Li are with Guangdong Provincial Key Laboratory of Optoelectronic Information Processing Chips and Systems, Sun Yat-Sen University, Guangzhou, China (e-mail: chenyy628@mail2.sysu.edu.cn; lzhh88@mail.sysu.edu.cn).

with an ultra-narrow linewidth laser and achieving a spatial resolution of 3.5 m over 40 km of fiber. However, phase demodulation-based systems usually require a well-designed receiving structure and signal processing progress to compensate for phase noise, which increases system complexity.

Methodologically, strain or dynamic strain induces a phase modulation of the phase term of the Rayleigh backscattered signal in terms of the physical mechanism, while phase demodulation or correlation demodulation observes the phase shifts at different domains. For phase demodulation schemes, since the phase term continuously increases over time, it must be normalized to the interval from -π to π using the arctangent function and unwrapping algorithms to reveal periodic characteristics like frequency and amplitude. However, phase hopping, caused by signal fading, can severely impact phase extraction stability [21]. Errors typically occur during phase unwrapping at the -π to π transition, limiting the maximum measurable strain to that which induces a differential phase of 2π between two adjacent samples, even without considering random phase hopping. In this respect, phase demodulation based OFDR systems are more sensitive and more likely to be affected by unexpected perturbations at the same time. Regarding correlation demodulation schemes, even though the cross-correlation scheme can mitigate the effects of random fading by dividing a sequence of local spectra, similar issue also exists, where wavelength shifts in the local Rayleigh backscattering spectra (RBS) exceed the sweeping range, leading to inaccurate cross-correlation results. Unreliable phase information or cross-correlation outcomes can introduce erroneous frequency components into the signal, potentially causing false alarms in the DAS system and introduce an unnecessary patrolling burden. Given these challenges, the development of a versatile and highly adaptive OFDR-based DAS system is warranted. From the perspective of this objective, the cross-correlation scheme focuses on localized information rather than single-point specific information, and a portion of the internal noise is suppressed, making it more robust and more promising for highly adaptive sensing. Although the spatial resolution of this scheme is not as good as the phase demodulation scheme, it is acceptable in long distance scenarios.

In this paper, we propose a novel DAS system based on short-chirped-pulse OFDR, combined with cross-correlation analysis, to localize and analyze vibration signals over a 32 km fiber with a spatial resolution of 14 m. This system outperforms conventional OFDR approaches by extending the measurement range through the use of a narrow linewidth laser and by enhancing noise tolerance and reducing complexity through the cross-correlation scheme, compared to phase demodulation methods. We also address the frequency demodulation distortion phenomenon that occurs under large unexpected vibrations for the first time. A new approach, termed negative quality factor (NQF) analysis, is introduced for selecting valid RBS shifts in combination with the cubic spline algorithm to recover the vibration. We demonstrate the effectiveness of this method under large vibration conditions and successfully refine the vibration frequency analysis.

II. Principle

A. RBS Shift-Based Stationary Measurement

Rayleigh scattering is a form of elastic scattering considered an inherent characteristic of optical fibers, stemming from the random distribution of the refractive index within the fiber. OFDR is adept at measuring Rayleigh backscattering, capturing it as a distributed reflectivity pattern along the length of the fiber under test (FUT). This pattern remains consistent in the absence of external environmental disturbances. However, when a perturbation occurs, changes in the refractive index become detectable through the RBS generated by the interaction between the signal light from the FUT and the reference light. For instance, the strain applied to the fiber results in a shift in the RBS, which can be quantified as follows [22],

$$\varepsilon = -0.78\,\delta\nu/\nu_0 \tag{1}$$

where ε is the applied axial strain, $\delta\nu$ is the RBS shift and ν_0 is the initial optical frequency.

To facilitate strain measurements, it is necessary to calibrate a reference RBS pattern under strain-free conditions. When strain is applied, the RBS measured at a specific location will be different from the reference RBS at the corresponding position. This variation is not easily discernible through simple visual inspection but can be detected through a complex cross-correlation operation. The RBS shift is calculated from the cross-correlation shift. Assuming that the optical frequency of the emitted light changes linearly over time, the symbols τ_1, τ_2, τ_3, and τ_4 represent the time delays of the same reflection point during four different tuning periods. By comparing the local RBS at this point at various times with the reference RBS, both the direction and magnitude of the strain can be determined. This process is illustrated in the diagram shown in Fig.1.

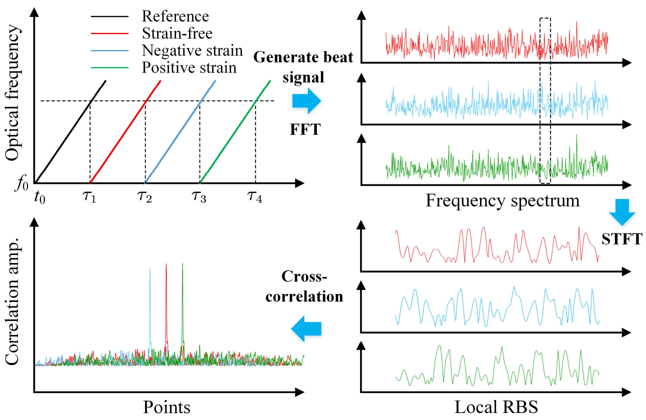

Fig. 1. Principle of RBS shift-based stationary measurement.

B. RBS Shift-Based Dynamic Measurement

As discussed in the Introduction, conventional TLS-based OFDR systems face limitations in dynamic measurement capabilities due to the duration of the probe light. Although the RBS shift-based method can be used for dynamic vibration measurement in principle, the frequency sweep rate of the TLS should be significantly increased, as this rate dictates the frequency response range of the DAS system. In the proposed OFDR-based DAS system, the use of short-chirped pulses enhances the system's ability to perform dynamic measurements.

Physically, vibration is fundamentally the periodic motion of an object or a part of an object around a position, characterized by periodicity, amplitude, and energy. In the context of optical fibers, vibration can be conceptualized as periodic dynamic strain. Thus, the theoretical model of vibration in an OFDR system is described from the perspective of strain. An OFDR system generates a beat signal through the optical interference between two light signals originating from the same light source. One signal is the Rayleigh backscattering or reflection light from the FUT, referred to as the measured light. The other signal, used for interference, is the forward light from the reference path, known as the reference light. Assuming a constant frequency sweep rate γ, the optical field $E_r(t)$ of the reference path can be expressed as follows,

$$E_r(t) = E_0 \exp\left\{j\left[2\pi\left(f_0 t + \tfrac{1}{2}\gamma t^2\right)\right]\right\} \tag{2}$$

where E_0 is the initial optical field and f_0 is the initial optical frequency. At this moment, the measured light $E_s(t)$ without strain imposed on the fiber can be written as,

$$E_s(t) = \sum_i \sqrt{R(\tau_i)}E_0 \cdot \exp\left\{j\left[2\pi\left(f_0(t-\tau_i)+\tfrac{1}{2}\gamma(t-\tau_i)^2\right)\right]\right\} \tag{3}$$

where i denotes the scatterer index distributed along the FUT, and $R(\tau_i)$ is the reflectivity with fiber attenuation of the FUT at the round-trip delay τ_i.

Then the beat signals with intensity $I(t)$ originating from the interference of the measured light and reference light are detected by the photodetector, which can be written as,

$$I(t) = \mathrm{Re}[E_r(t)\times E_s^*(t)] = \textstyle\sum_i \sqrt{R(\tau_i)}E_0^2 \cos\left\{\left[2\pi\left(f_0\tau_i+\gamma\tau_i t-\tfrac{1}{2}\gamma{\tau_i}^2\right)\right]\right\} \tag{4}$$

where Re [] denotes taking the real part of complex data, * is the symbol of complex conjugation.

After data acquisition, the Fourier transform is applied to convert time-domain data into frequency-domain (distance-domain) data. This distance-domain data can be segmented to analyze specific regions along the FUT, akin to the process of windowing. Through this method, the spatial resolution of the system is defined as the spatial distance that corresponds to the size of the window. Subsequently, complex time-domain data $I_c(t)$ can be retrieved by performing an inverse Fourier transform on the data within the selected window,

$$I_c(t) = \sum_{i=n}^{m} \sqrt{R(\tau_i)}E_0^2 \cdot \exp\left\{j\left[2\pi\left(f_0\tau_i+\gamma\tau_i t-\tfrac{1}{2}\gamma{\tau_i}^2\right)\right]\right\} \tag{5}$$

where n and m are the start and end points of the window. Equation (5) represents the case without external strain. Considering a stable strain applied in this region, a phase of δ will be introduced to the RBS, and the modulated measured light $E_s'(t)$ can be written as follow,

$$E_s'(t) = \sum_{i=n}^{m} \sqrt{R(\tau_i)}E_0 \cdot \exp\left\{j\left[2\pi\left(f_0(t-\tau_i)+\tfrac{1}{2}\gamma(t-\tau_i)^2\right)-\delta\right]\right\} \tag{6}$$

Assuming that a periodically varying strain is applied, i.e., a vibration, then the phase modulation could be written as $\delta\sin(2\pi f_v t)$, where f_v is the characteristics frequency of the varying strain and δ is the phase modulation amplitude. Using $E_v'(t)$ to denote the measured light in the vibration case, then (6) can be rewritten as,

$$E_v'(t) = \sum_{i=n}^{m} \sqrt{R(\tau_i)}E_0 \cdot \exp\left\{j\left[2\pi\left(f_0(t-\tau_i)+\tfrac{1}{2}\gamma(t-\tau_i)^2\right)-\delta\sin 2\pi f_v t\right]\right\} \tag{7}$$

As mentioned in (1), the modulated phase δ results in RBS shift can be expressed as $\delta\nu = -\frac{\varepsilon\nu_0}{0.78}$. Therefore, it logically follows that the RBS shift due to the modulated phase under vibration conditions can be expressed as,

$$\delta\nu(t) = -\varepsilon\sin(2\pi f_v t)\nu_0/0.78 \tag{8}$$

In practice, the amplitude of the RBS shift $\delta\nu(t)$ would be smaller than (8) due to the presence of damping, but the linear relationship still holds. In a word, the frequency of the varying RBS shift follows the frequency of the applied vibration, while the variation's amplitude relatively reflects the intensity of the vibration.

C. *RBS Shift-based Dynamic Acoustic Measurement Operation Process*

Building on the discussions above, the process of reconstructing the vibration signal from the RBS shift is depicted in Fig.2.

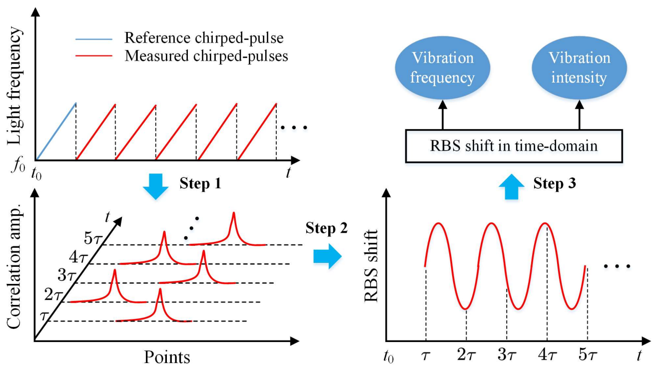

Fig. 2. Schematic of the RBS shift-based dynamic acoustic measurement process.

Step 1: Analogous to stationary measurements, the local RBS spectra at a specific location for different time instances are first acquired using Fast Fourier Transform (FFT) and Short-Time Fourier Transform (STFT). Subsequently, cross-correlation is performed between the measured chirped pulses and the reference chirped pulse to obtain the correlation results.

Step 2: The RBS shifts for various chirped-pulse intervals are determined from the cross-correlation outcomes. These shifts are then chronologically arranged to form the RBS shift distribution.

Step 3: The RBS shift distribution is analyzed to fit the data, which allows for the extraction of the frequency and amplitude of the RBS shift variations. These parameters correspond to the vibration frequency and intensity, respectively.

D. Discussion on the dynamic acoustic measurement performance

1) Spatial Resolution

Similar to stationary measurements, the spatial resolution Δx of the proposed DAS system, facilitated by the use of STFT, can be expressed as,

$$\Delta x = N\Delta z \tag{9}$$

and

$$\Delta z = c/2n\Delta F \tag{10}$$

where N is the width of the sliding window, c is the speed of light, n is the effective refractive index, and Δz is the theoretical spatial resolution of the system, which depends on the sweeping range ΔF.

2) Measurement Range

First, the system's measurement range is constrained by the coherence length of the laser due to the coherent detection scheme. While ensuring that the coherence length is adequate, it is also essential to ensure that the frequency-swept light within a chirped-pulse covers every point on the FUT. Assuming the width of the chirped-pulse is τ, the maximum measurement range can be expressed as,

$$L_{\max} = c\tau/2n = c\Delta F/2n\gamma \tag{11}$$

where γ is the frequency-swept rate of the chirped-pulse.

3) Frequency Response Range

The repetition rate of the chirped-pulses determines the upper limit of the frequency response. The theoretical maximum frequency response is approximately half of the repetition rate. The lower boundary is contingent on the number of chirped-pulses utilized.

4) Intensity Response Range

Considering vibrations as periodic dynamic strains, the intensity response of vibrations can be interpreted in terms of strain sensing capability. On one hand, the strain-induced RBS shift cannot exceed the sweeping range ΔF. On the other hand, the smallest detectable RBS shift $\delta v_{\min}$ is influenced by the width of the sliding window N, which can be formulated as,

$$\delta v_{\min} = \Delta F/N \tag{12}$$

As previously mentioned, within a given sweeping range, the intensity response range of vibrations may be more limited than the strain response range due to damping effects. Nonetheless, it is still governed by ΔF and N. If ΔF, is insufficient, it may lead to the inability to calculate the RBS shift at certain times, causing errors in the vibration frequency demodulation. This phenomenon will be discussed in subsequent sections.

E. The Negative Quality Factor (NQF) Analysis

As forementioned, the RBS shift is obtained by cross-correlation. The detained function can be defined as,

$$R_{rs}(\tau) = \sum_{n=-(N-1)}^{N-1} r[n]s[n+\tau] \tag{13}$$

where $r[n]$ is local reference spectrum, $s[n]$ is local measured spectrum, and N is the length of local spectra. Then, a normalization of the computed R_{rs} is performed to facilitate the subsequent analyses.

Typically, the cross-correlation result with a sharp dominant peak is desired, which means the correlation between the two spectra is clear. However, the practical cross-correlation results are adversely affected by low SNR Rayleigh backscattering signals or large strains, resulting in pseudo-peak or multiple-peak patterns [23]. Based on this phenomenon, the NQF is defined to assess the clearness or reliability of the cross-correlation.

$$NQF = M_{thre}/M \tag{14}$$

where M_{thre} and M are the points above the threshold and the total points in the cross-correlation results, respectively. The threshold ranges from 0 to 1; usually, it should be greater than 0.5 (corresponding to an attenuation of 3dB). Both multiple peaks or broadening peaks cause a significant increase in the NQF level, so the NQF level is negatively correlated with the reliability of the RBS shift.

III. Experimental Setup

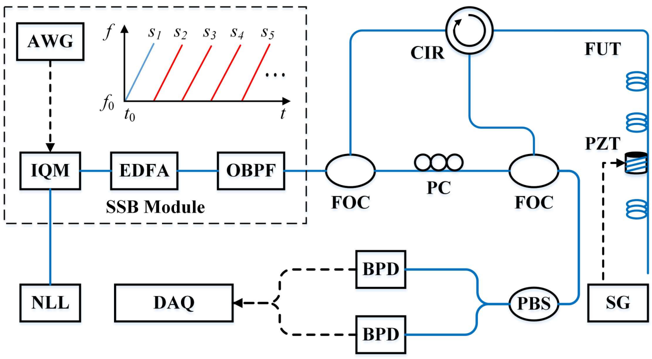

Fig. 3. Configuration of the proposed DAS system.

The configuration of the DAS system is illustrated in Fig.3. The narrow linewidth laser (NLL) (NKT: BASIK X15) emits highly coherent continuous-wave (CW) light with a linewidth of up to 100 Hz, which ensures an adequate coherence length. The NLL has a central wavelength of 1550.1 nm and an output optical power of 13 dBm. The CW light is then modulated by a single-sideband (SSB) modulation module to produce a series of continuous chirped-pulses (S_1-S_n) with carrier suppression, where S_1 serves as the initial chirped-pulse and acts as a reference for cross-correlation. The SSB modulation module comprises an arbitrary waveform generator (AWG) (Keysight: M8195A), an IQ modulator (IQM), an erbium-doped fiber amplifier (EDFA), and an optical bandpass filter (OBPF). The

EDFA boosts the optical power to extend the measurement range. The chirped-pulse light is then directed into a fiber optic coupler (FOC). The light in the upper branch is routed through a circulator to enter the FUT and generate the measured light. In the lower branch, the light passes through a polarization controller (PC) and serves as the reference light, which interferes with the measured light. The resulting beat signal is then split by a polarization beam splitter (PBS) into two orthogonally polarized components, which are detected by balanced photodetectors (BPD) for data acquisition (DAQ). A polarization diversity reception scheme is employed to mitigate the effects of polarization fading.

Regarding the FUT, it is composed of three fiber segments arranged sequentially: two 6 km segments followed by a 20 km segment. A piezoelectric transducer (PZT) wrapped with a 15m section of fiber is positioned between the second and third fiber segments to generate vibration signals. These vibration signals are simulated by sinusoidal signals produced by a signal generator (SG).

The detailed system parameters are as follows: The frequency sweep range and period of the chirped-pulses are 400 MHz and 0.4 ms, respectively. This implies that the frequency sweep rate of the chirped pulses is 1 THz/s, and their repetition rate is 2.5 kHz. According to (11), the maximum measurement range is 40 km, which ensures that the FUT is within the effective gauge range. Given the length of the FUT, the maximum beat frequency is approximately 320 MHz. The sampling rate of the DAQ device is set to 2 GS/s, which means that a single sweep period captures 800,000 data points. During signal processing, to mitigate potential frequency instabilities at the start and end of the chirped-pulse, only the central 700,000 points are utilized. As a result, the actual frequency sweep range utilized is 350 MHz. According to the setting parameters, it can be calculated that the theoretical spatial resolution is about 0.28 m if the sliding window is not taken into account. A 100-point sliding window with a 50% overlap was adopted in the experiments, so the actual expected spatial resolution is around 14 m refer to (9).

IV. Results and Discussions

In the experiments, sinusoidal signals with varying frequency were applied to the PZT via the SG. The frequency and voltage of the sinusoidal signal represent the frequency and intensity of the vibration.

A. Verification of the Spatial Resolution and the Frequency Response Capability

To verify the frequency response of the system, the maximum vibration frequency was set to 1 kHz, closely approaching the theoretical maximum frequency (1.25 kHz) detectable by the system. To illustrate the time-domain distribution of RBS shift, fifty chirped-pulses were used as references. Initially, fifty traces of RBS shift along the FUT are depicted in Fig.4(a). Notably, significant fluctuations in RBS shift are observed at 12.53 km, the location where the vibration signal was applied, as detailed in Fig.4(b). The spatial resolution is determined by the full width at half maximum (FWHM) of the RBS shift peaks, which, in this instance, is 14 m. It can be seen that the measured spatial resolution values agree with the theoretical ones. Subsequently, fifty distance-time mapping traces of RBS shift focusing on the vicinity of the vibration site are compiled and presented in Fig.5 to further show the time-frequency characteristics of the vibrations.

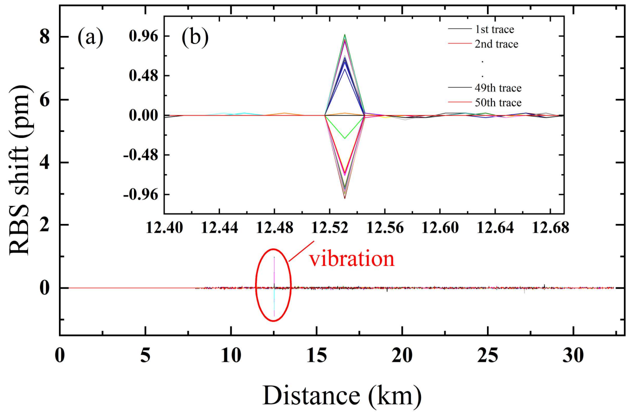

Fig. 4. (a) Fifty RBS shift traces distributed with distance; (b) Local RBS shift traces around vibration position.

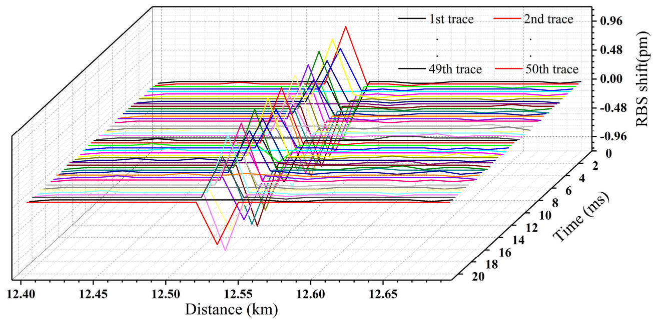

Fig. 5. Fifty distance-time mapping traces of RBS shift zooming around the vibration position.

The frontal view of the three-dimensional mapping corresponds to the subfigure Fig.4(b), illustrating frequent RBS shifts near the vibration site. This information can indicate the occurrence of a vibration event. Moreover, the side view of the three-dimensional mapping is shown in Fig.6(a), revealing the temporal trend of the RBS shift distribution, which aids in determining the vibration frequency and intensity. In this scenario, a vibration event near 12.53 km with a frequency of approximately 1000 Hz is evident, as highlighted in Fig.6(b). Fairly, the spectra broadening is somehow apparent due to the vibration's frequency being close to the upper limit of the system. However, it is consistent with sampling theory. These findings align with the experimental setup, thereby confirming the vibration sensing capabilities of the proposed system. It is worth noting that the minimum detectable frequency is contingent upon the signal length, i.e., the number of chirped-pulses used. Specifically, lower vibration frequencies necessitate a greater number of chirped-pulses to accurately capture the variation in RBS shift. Owing to the robust stationary measurement performance of the OFDR system based on correlation analysis, the lower frequency limit detectable by this study was not further investigated.

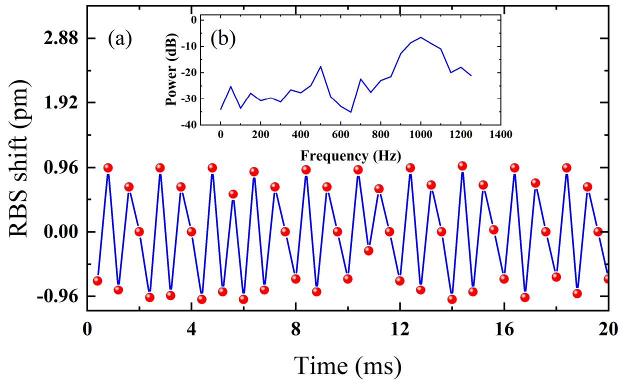

Fig. 6. (a) RBS shift distribution over time at the vibration position; (b) The power spectrum density of the vibration.

B. *Investigation of the Vibration intensity sensing capability*

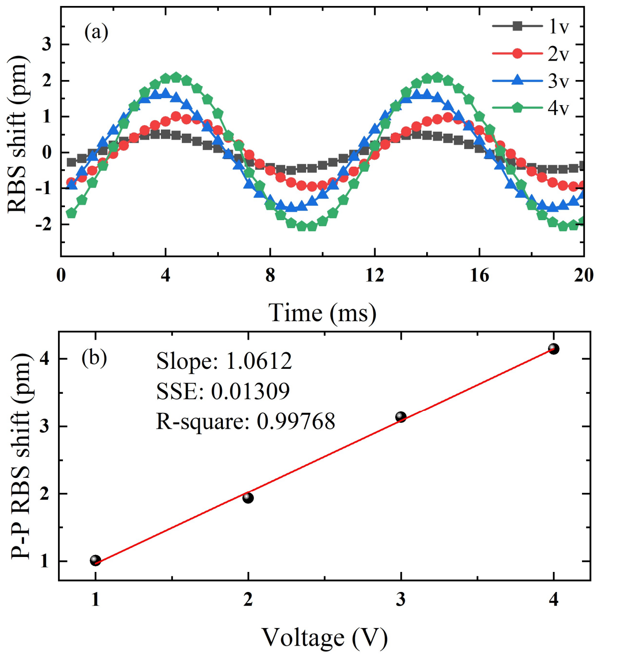

Fig. 7. (a) RBS shifts under different voltages; (b) P-P RBS shift as a function of applied voltage.

Fixing a constant frequency and applying different voltages to verify the intensity sensing performance. The experimental results for sensing a 100 Hz vibration under varying voltages (1V-4V) are depicted in Fig.7(a). The four RBS shift curves exhibit periodic changes over two cycles within 20 ms, indicating a vibration frequency of approximately 100 Hz. To determine the calibration coefficient of peak-to-peak (P-P) RBS shift relative to the applied PZT voltage, linear fitting was applied to the curve of P-P RBS shift versus PZT applied voltage. The results, shown in Fig.7(b), reveal a strong linear relationship between these two variables, agreeing with (8). The linear regression analysis yielded a sum of squares due to error (SSE) of 0.01309, an R-square of 0.99768, and a calibration coefficient of 1.0612 pm/V. It is worth noting that the experimental conditions in this section ensured that the RBS shifts did not exceed the sweeping range.

C. *Investigation of the Vibration Frequency Sensing Capability*

With a fixed applied PZT voltage of 1 V, the RBS shifts for vibration frequencies ranging from 100-800 Hz are illustrated in Fig.8(a)-(f), with the corresponding power spectra of FFT shown in Fig.8(g). The applied frequencies are accurately extracted with a high SNR of about 30 dB. The P-P RBS shifts appear to be nearly independent of frequency, all fluctuating between -0.5 and 0.5, consistent with theoretical predictions. In summary, these results affirm the exceptional vibration frequency sensing capability of the proposed OFDR-based DAS system.

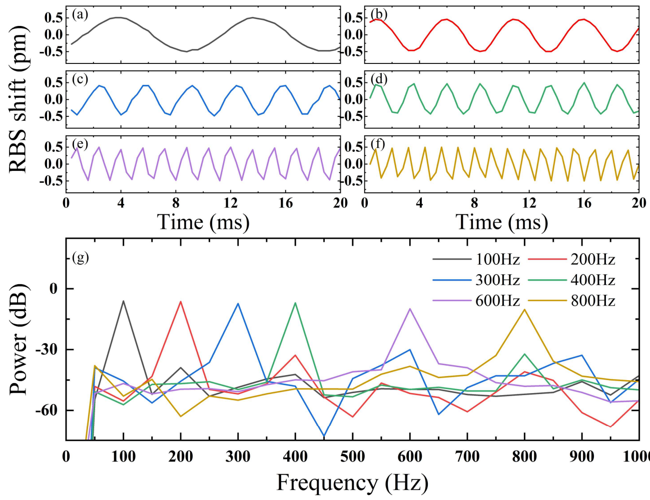

Fig. 8. RBS shifts for vibration frequencies of 100-800 Hz: (a) RBS shift of 100 Hz; (b) RBS shift of 200 Hz; (c) RBS shift of 300 Hz; (d) RBS shift of 400 Hz; (e) RBS shift of 600 Hz; (f) RBS shift of 800 Hz; (g) The corresponding power spectra of FFT.

D. *Investigation of the Frequency Demodulation Error due to Insufficient Sweeping Range*

As discussed in the section on intensity response range, an inadequate sweeping range can cause failures in cross-correlation calculations at certain times, leading to errors in vibration frequency demodulation. Due to the AWG's memory depth limitations, there's a trade-off between the repetition rate and the sweeping range of chirped-pulses. Achieving a high repetition rate and a large sweeping range simultaneously is challenging under the external modulation scheme. This study prioritizes the repetition rate to showcase dynamic performance. Fortunately, dynamic measurements focus on trends in RBS shift changes rather than precise numerical values, allowing for signal restoration despite partial point distortions. To illustrate, consider the following examples.

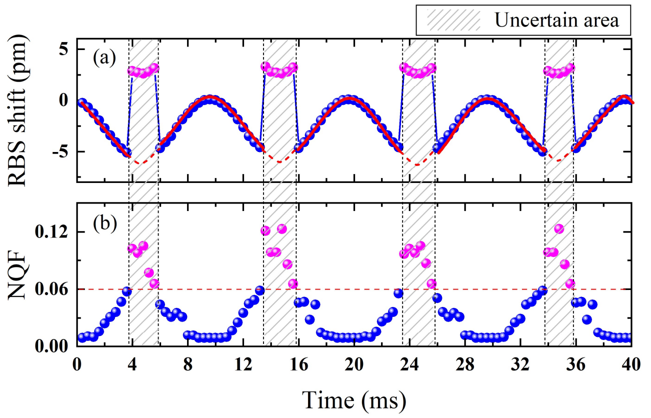

Fig. 9. (a) RBS shift trace for a 5 V sinusoidal signal (100 Hz); (b) NQF trace for a 5 V sinusoidal signal (100 Hz).

Applying a 100 Hz sinusoidal signal at 5 V to the PZT results in a calculated P-P RBS shift of 5.306 pm, close to the maximum P-P RBS shift of 5.6 pm. Considering damping effects, the actual limit is likely below 5.6 pm, posing a risk of exceeding the sensing capacity. As shown in Fig. 9(a), the RBS shift trace for 100 chirped-pulses shows a quasi-sinusoidal distribution of data within the range (-5.1 to 0.1 pm), with biased data occurring in the uncertain area. Despite these deviations, the RBS shift indicates a vibration frequency of 100 Hz over 4 cycles in 40 ms. Here, we artificially chose an initial moment so that the RBS shift trace could fully display the upper or lower envelope of the curve, thus determining that the system perceived a sinusoidal signal. It also explains why the RBS shift trace is not symmetrically distributed about the zero point. The uncertainty observed can be anticipated from the cross-correlation results. Take one point (25^{th}) on the sine curve (corresponding to 10 ms) and another point (34^{th}) off the curve (corresponding to 13.6 ms) as a reference, their the cross-correlation results are shown in Fig.10(a) and Fig.10(b), respectively.

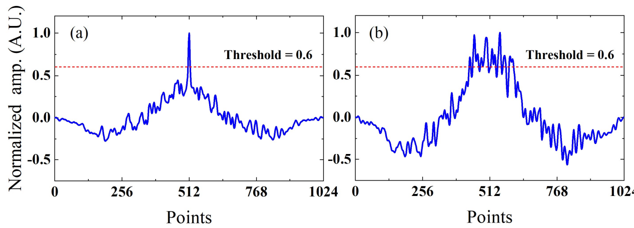

Fig.10. (a) Cross-correlation result of the 25^{th} data point; (b) Cross-correlation result of the 34^{th} data point.

Figure 10(a) shows a dominant peak, whereas Fig.10(b) displays several elevated peaks. Note that the width of the window after zero-padding in the STFT is 512, so there are 1024 points in the horizontal coordinates in the cross-correlation result. Defining the cross-correlation NQF as the proportion of points exceeding a threshold in the normalized amplitude curve, with a threshold value of 0.6 based on pre-experiments, a high NQF indicates increased uncertainty in the cross-correlation results. The NQF trace in Fig.9(b) correlates with the uncertain areas in Fig.9(a), highlighting data points with high NQF levels. In the signal process, these high NQF points can be easily filtered by a conditional loop function. In this case, the filtering condition could be whether the NQF level is greater than 0.06.

Applying a 100 Hz sinusoidal signal at 7.5 V to the PZT, as shown in Fig.11(a), results in more data points deviating from the quasi-sine curve, with corresponding high NQF levels in Fig.11(b). Similarly, whether the NQF level is greater than 0.06 can still be used as a reference. This demonstrates that NQF can also reflect the reliability of RBS shift results in more extreme cases.

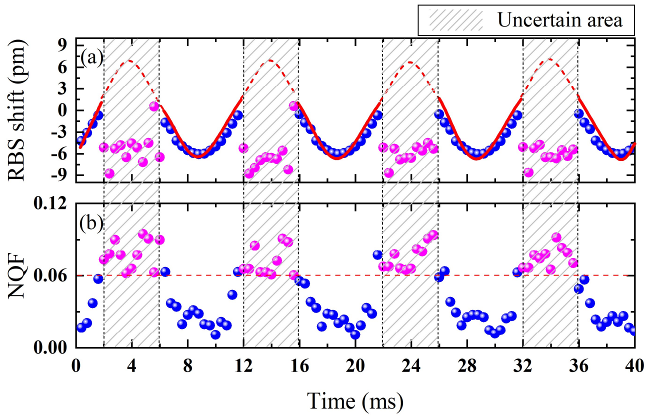

Fig. 11. (a) RBS shift trace for a 7.5 V sinusoidal signal (100 Hz); (b) NQF trace for a 7.5 V sinusoidal signal (100 Hz).

For comparison, a 100 Hz sinusoidal signal with a voltage of 1 V is applied to the PZT. As shown in Fig.12(a), the RBS shift fluctuates with a sinusoidal pattern between -0.5 and 0.5 pm. Since the intensity response of the DAS system is sufficient in this case, the RBS shift trace is smooth and complete. At the same time, it can be seen from Fig.12(b) that the corresponding NQF remains at a fairly low level, no more than 0.02. Compared to the case of 5 V, the value of the NQF is so low that all RBS shift data points are trustworthy at this point. The case further supports the reliability of using the NQF to evaluate the quality of the RBS shift.

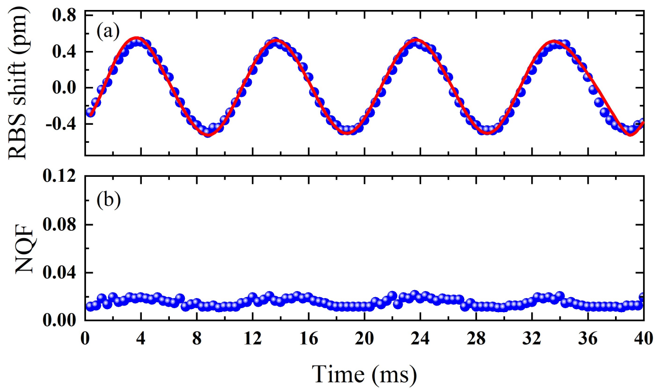

Fig. 12. (a) RBS shifts trace for a 1V sinusoidal signal (100 Hz); (b) NQF trace for a 1V sinusoidal signal (100 Hz).

E. *Investigation of the Adaptive Sensing Capability*

Take the case of applying a 100 Hz (7.5V) sinusoidal signal to investigate the adaptive sensing capability of the proposed scheme.

TABLE I: Comparison among the OFDR-based DAS systems and the proposed system.

Work	Configuration	Range	Spatial resolution	Maximum measured frequency/Pulse rate	SNR	Over-range intensity response capability
Ref. [18]	TLS-based	17 m	10 cm	32 Hz/64 Hz	N.A.	N.A.
Ref. [19]	TLS-based	12 km	5 m	2 kHz/3.2 kHz	N.A.	N.A.
Ref. [20]	External modulation (TGD-OFDR)	40 km	3.5 m	600 Hz/2 kHz	3 dB	N.A.
Ref. [24]	External modulation (TFM-OFDR)	1 km	22 cm	10.5 kHz/100 kHz	20 dB	N.A.
This work	External modulation (Short-chirped-pulse OFDR)	32 km	14 m	1 kHz/2.5 kHz	30 dB	Verified

The adaptive correction process mainly consists of the following steps:

Step 1: Obtain the raw RBS shift, store it in array R as shown in Fig.13(a), and compute the corresponding NQF array Q.

Step 2: Use a conditional loop to search for the index of the elements in Q that is less than 0.6, then keep only the corresponding elements in R and generate a new array R_1 presented in Fig.13(b). By this mean, the low reliability RBS shift points have been filtered.

Step 3: Perform cubic spline interpolation on R_1 to restore the complete RBS shift array R_2 as plotted in Fig.13(c). Here, the corrected RBS shifts are obtained. Then FFT is performed on R_2 to acquire its power spectrum density for further analysis.

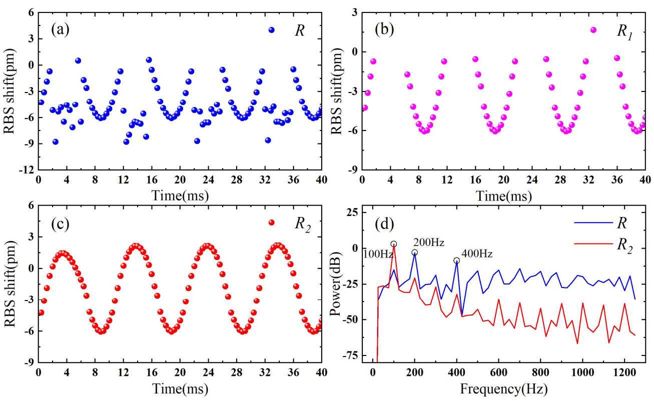

Fig. 13. (a) Raw RBS shifts R; (b) Selected high reliability RBS shifts R_1; (c) Restored RBS shifts R_2; (d) The power spectrum density of R and R_2.

The power spectrum of the RBS shift before and after correction is shown in Fig.13(d), which indicates the frequency characteristics of the vibration signals sensed by the DAS system. It can be seen that several higher and false frequency components appear without correction, especially 200 Hz and 400 Hz, while the true vibration frequency of 100 Hz is drowned out. In contrast, it is clear after the correction that the vibration signal has a specific frequency of 100 Hz and a SNR of up to 25 dB. The average noise level is also significantly reduced. The case demonstrated a potential dilemma for a DAS system when unexpected large vibrations occur. In this situation, the insufficient intensity sensing capability leads to an erroneous vibration alarm. By the proposed adaptive correction scheme, the real vibration signal is successfully restored, breaking the limitation of intensity sensing capability. The comparison of the existing works with the proposed work is displayed in Table I, to give a comprehensive picture of the performances of the different schemes.

In conclusion, referring to the NQF allows for the identification of reliable data points in the RBS shift trace, facilitating the determination of vibration frequency. However, accurately demodulating vibration when its intensity significantly exceeds the sensing capacity remains challenging. Under such conditions, the DAS system functions more like a DVS, capable of detecting vibration presence without detailed vibration information.

V. Conclusion

In this paper, we propose a DAS system based on short-chirped pulses OFDR. By ordering the RBS shift generated by a series of short-chirped pulses in time, the trace of the RBS shift is obtained using the cross-correlation operation, so the frequency and intensity of the RBS shift variation can be further determined. By theoretical derivation, a conclusion is drawn that a linear relationship exists between the frequency and amplitude of the RBS shift variation and the frequency and intensity of vibration events, respectively. In the experiment, the maximum vibration frequency of up to 1 kHz is demonstrated over the 32 km FUT with a SNR of up to 30 dB and a spatial resolution of 14 m. Moreover, the linear relationship was successfully verified, proving the feasibility of the scheme. In addition, the system's vibration sensing performance under unexpected large vibrations is discussed. To shield against the pseudo-RBS shifts, we propose to utilize the NQF of the cross-correlation results to evaluate the reliability of the RBS shifts, and then restoring the vibration information using the highly reliable RBS shift data points in combination with the cubic spline interpolation algorithm.

References.

[1] G. Marra et al., "Optical interferometry–based array of seafloor environmental sensors using a transoceanic submarine cable," *Science*, vol. 376, no. 6595, pp. 874-879, 2022.

[2] H.-N. Li, D.-S. Li, and G.-B. Song, "Recent applications of fiber optic sensors to health monitoring in civil engineering," *Eng. Struct.*, vol. 26, no. 11, pp. 1647–1657, 2004.

[3] X. Bao and L. Chen, "Recent progress in distributed fiber optic sensors," *Sensors*, vol. 12, no. 7, pp. 8601-8639, 2012.

[4] N. J. Lindsey, "Geophysical applications of ϕ-OTDR/DAS," in Optical Fiber Communication Conference (OFC), 2023.

[5] C. Fan, H. Li, T. He, S. Zhang, B. Yan, Z. Yan, and Q. Sun, "Large dynamic range optical fiber distributed acoustic sensing (DAS) with differential-unwrapping-integral algorithm," *J. Lightw. Technol.*, vol. 39, no. 22, pp. 7274-7280, 2021.

[6] Z. Li, J. Zhang, M. Wang, Y. Zhong, and F. Peng, "Fiber distributed acoustic sensing using convolutional long short-term memory network: a field test on high-speed railway intrusion detection," *Opt. Exp*., vol. 28, no. 3, pp. 2925-2938, 2020.

[7] C. Fan, H. Li, B. Yan, Y. Sun, T. He, T. Huang, Z. Yan, and Q. Sun, "High-precision distributed detection of rail defects by tracking the acoustic propagation waves," *Opt. Exp*., vol. 30, no. 22, pp. 39283-39293, 2022.

[8] F. Peng, H. Wu, X. Jia, Y. Rao, Z. Wang, and Z. Peng, "Ultra-long high-sensitivity Φ-OTDR for high spatial resolution intrusion detection of pipelines," *Opt. Exp*., vol. 22, no. 11, pp. 13804-13810, 2014.

[9] B. Yan, H. Li, K. Zhang, X. Xiao, T. He, C. Fan, Z. Yan, and Q. Sun, "Quantitative identification and localization for pipeline microleakage by fiber distributed acoustic sensor," *J. Lightw. Technol.*, vol. 41, no. 16, pp. 5460-5467, 2023.

[10] H. Gemeinhardt and J. Sharma, "Machine-learning-assisted leak detection using distributed temperature and acoustic sensors," *IEEE Sensors J.*, vol. 24, no. 2, pp. 1520-1531, 2024.

[11] Y. Wang, B. Jin, Y. Wang, D. Wang, X. Liu and Q. Bai, "Real-time distributed vibration monitoring system using Φ-OTDR," *IEEE Sensors. J.*, vol. 17, no. 5, pp. 1333-1341, 2017.

[12] Yoshifumi Wakisaka, Hiroshi Takahashi, Daisuke Iida, and Yusuke Koshikiya, "Broad-bandwidth and accurate optical vibration sensing by using FDM Φ-OTDR with linear regression analysis of multi-frequency phase responses," *Opt. Exp*., vol. 31, no. 17, pp. 27990-28009, 2023.

[13] H. F. Martins, S. Martín-López, P. Corredera, M. L. Filograno, O. Frazão and M. Gonzalez-Herráez, "Phase-sensitive optical time domain reflectometer assisted by first-order Raman amplification for distributed vibration sensing over >100 km," *J. Lightw. Technol.*, vol. 32, no. 8, pp. 1510-1518, 2014.

[14] Hari Datta Bhatta, Luis Costa, Andres Garcia-Ruiz, Maria R. Fernandez-Ruiz, Hugo F. Martins, Moshe Tur, and Miguel Gonzalez-Herraez, "Dynamic measurements of 1000 microstrains using chirped-pulse phase-sensitive optical time-domain reflectometry," *J. Lightw. Technol.*, vol. 37, no. 18, pp. 4888-4895, 2019.

[15] Z. Wang, J. Zeng, J. Li, M. Fan, H. Wu, F. Peng, L. Zhang, Y. Zhou, and Y. Rao, "Ultra-long phase-sensitive OTDR with hybrid distributed amplification," *Opt. Lett.*, vol. 39, no. 20, pp. 5866-5869, 2014.

[16] Enrique Piñeiro, Mikel Sagues, and Alayn Loayssa, "Compensation of phase noise impairments in distributed acoustic sensors based on optical pulse compression time-domain reflectometry," *J. Lightw. Technol*., vol. 41, no. 10, pp. 3199-3207, 2023.

[17] W. Feng, M. Wang, H. Jia, K. Xie, and G. Tu, "High precision phase-OFDR scheme based on fading noise suppression," *J. Lightw. Technol*., vol. 40, no. 3, pp. 900-908, 2022.

[18] D. Zhou, Z. Qin, W. Li, L. Chen, and X. Bao, "Distributed vibration sensing with time-resolved optical frequency-domain reflectometry," *Opt. Exp*., vol. 20, no. 12, pp. 13138-13145, 2012.

[19] Z. Ding, X. Yao, T. Liu, Y. Du, K. Liu, Q. Han, Z. Meng, and H. Chen, "Long-range vibration sensor based on correlation analysis of optical frequency-domain reflectometry signals," *Opt. Exp*., vol. 20, no. 27, pp. 28319-28329, 2012.

[20] S. Wang, X. Fan, Qi. Liu, and Z. He, "Distributed fiber-optic vibration sensing based on phase extraction from time-gated digital OFDR," *Opt. Exp*., vol. 23, no. 26, pp. 33301-33309, 2015.

[21] M. Zhao, G. Tu, B. Yu, and J. Lin, "The analysis and comparison of cross-correlation and phase demodulation methods in an OFDR system for strain/temperature sensing," *Proc. SPIE*, vol. 10821, Art. no. 1082125, 2018.

[22] Y. Koyamada, M. Imahama, K. Kubota, and K. Hogari, "Fiber-optic distributed strain and temperature sensing with very high measurand resolution over long range using coherent OTDR," *J. Lightw. Technol*., vol. 27, no. 9, pp. 1142-1146, 2009.

[23] C. Shao et al., "OFDR with local spectrum matching method for optical fiber shape sensing," *Appl. Phys. Express*, vol. 12, pp. 082010, 2019.

[24] Zixuan Zhong, Tao Liu, Haoting Wu, Junjie Qiu, Boyang Du, Guolu Yin, and Tao Zhu, "High-spatial-resolution distributed acoustic sensor based on the time-frequency-multiplexing OFDR," *Opt. Lett*., vol. 48, pp. 5803-5806, 2023.